Structural Insights into Photoactivation of Plant Cryptochrome-2

Malathy Palayam[1,2†], Jagadeesan Ganapathy[1†], Angelica M. Guercio[1†], Lior Tal[1], Samuel L. Deck[1], and Nitzan Shabek[1*]

[1]*Department of Plant Biology, University of California – Davis, Davis, CA 95616*

[2]*Department of Chemistry, University of California – Davis, Davis, CA 95616*

[†]*Equal contribution*

[*]*Correspondence should be addressed to: nshabek@ucdavis.edu*

Abstract

Cryptochromes (CRYs) are evolutionarily conserved blue-light receptors that mediate various light-induced responses in bacteria, plants, and animals. Plant cryptochromes govern a variety of critical growth and developmental processes including seed germination, flowering time and entrainment of the circadian clock. CRYs photocycle involves reduction of their flavin adenine dinucleotide (FAD)-bound chromophore, which is completely oxidized in the dark and semi-reduced in the light signalling-active state. Despite the significant progress in characterizing cryptochromes, important aspects of their photochemistry, regulation, and light-induced structural adaptation remain to be addressed. In this study, we determine the crystal structure of the photosensory domain of Arabidopsis CRY2 in a tetrameric active state. Systematic structure-based analyses of photo-activated and inactive plant CRYs elucidate new structural elements and critical residues that dynamically partake in photo-induced oligomerization. Our study offers an updated model of CRYs photoactivation mechanism as well as the mode of its regulation by interacting proteins.

Introduction

Cryptochromes (CRYs) are evolutionarily conserved blue-light photoreceptors that regulate numerous developmental networks including de-etiolation, photoperiodic control of flowering, root growth, plant height, organ size, stomatal opening, and stress responses[1-5]. Plants encode three different CRYs (CRY1-3); CRY1 and CRY2 function in the nucleus and predominantly regulate seedling development and flowering time, while CRY3 mostly functions in subcellular organelles[5-7]. CRYs are comprised of two core domains: the highly conserved N-terminal photolyase homologous region (PHR) and the diversified carboxy-terminal extension (CCE). The PHR domain is further subdivided into N-terminal α/β and C-terminal α subdomains[8-10]. The chromophore, flavin adenine dinucleotide (FAD), is non-covalently bound to the C-terminal α subdomain of the PHR and play a critical role in facilitating photoreduction[11-15]. Therefore, the PHR domain serves as the core function of the light sensing mechanism of cryptochromes. Unlike the conserved PHR structure, the CCE domain is disordered and varies in length, yet it plays essential roles in the light signaling pathway including the direct interaction and regulation by the COP1 E3 ubiquitin ligase[16-19]. CRYs photocycle involves redox changes of FAD, which is completely oxidized in the dark and semi-reduced in the light signaling-active state. The PHR domain contains three conserved tryptophan residues referred to as "Trp-triad" that were proposed to function in CRYs photoreduction[20,21]. It has been suggested that upon exposure to blue light, electron transfer through the tryptophan residues reduce the oxidized FAD to FADH[22,23]. The aspartic residue adjacent to the isoalloxazine ring of FAD has been shown to have a critical role in coordinating FAD photocycle by acting as the proton donor[24]. Despite the biochemical data, the function of tryptophan residues *in planta* has been questioned after showing that the Trp triad-dependent photoreduction may not be required for the photo-physiological activities of CRYs[25].

Hence the photoactivation mechanism of CRYs and how the photocycle triggers conformational changes remain to be addressed[11,12,26]. It has been largely accepted that blue light induces the homo-oligomerization of plant CRYs and the oligomer represents the activated state whereas the monomer exhibits the inactivate state[27-29]. In addition, CRYs oligomerization was found to be regulated by protein interactions with various signaling partners such as bHLH inhibitor of cryptochrome (BIC)s and CIBs transcription factors[30,31]. Recently, the structure of PHR domain of Arabidopsis CRY2 has been determined as a monomer as well as in a complex with BIC2[32]. These structures provide important insights into the mechanism by which the inhibitor BIC2 binds to and regulates cryptochromes. Moreover, the oligomeric structure of bioactive *Zea mays* mutant CRY1 (*Zm*CRY1C^{W374A}) has been reported and proposed a mechanism for photo-activated CRYs[16]. Despite the significant progress in characterizing and understanding the photo-oligomerization of CRYs at the structural levels, a high-resolution structure of wild-type plant CRY2 in the oligomeric activated state has yet to be determined, and detailed analysis of light-induced structural adaptation remains to be addressed.

Here, we report the crystal structure of Arabidopsis CRY2 PHR domain in a tetrameric active state. Our systematic structure-based analyses of photo-activated and inactive BICs-CRYs identified new structural elements and critical residues that dynamically partake in photo-induced oligomerization. Furthermore, comparative conformational examination suggests that the tetrameric CRY2 recapitulates an intermediate state of electron transport *via* the Trp-triad. Our study offers an important updated model of CRYs photoactivation mechanism as well as the mode of its regulation by interacting proteins.

Results

Crystal structure of tetrameric Arabidopsis CRY2

To examine the oligomeric structure of photoactivated CRY2, we expressed, purified and crystalized the complete PHR domain of wild-type Arabidopsis CRY2. Following extensive crystallization trials under light conditions, we successfully determined the crystal structure of Arabidopsis CRY2 in a tetrameric state (denoted *At*CRY2$_t$, where subscript t indicates tetrameric structure). *At*CRY2$_t$ is comprised of four monomeric units (A, B, C, D) that are arranged as a ring-like structure with a central hollow cavity **(Figure 1a** and **Table 1)**. The tetrameric conformation of *At*CRY2$_t$ is related by two-fold symmetry with overall size of 110.5^{2}Å **(Figure 1a)**. Each individual unit of the PHR domain is comprised of an N-terminal α/β domain (residues 5-132), C-terminal α domain (residues 214-487) and a connector loop (residues 133-213) which links the domains together **(Figure 1b** and **Figure S1)**. The co-factor, FAD, adopts a typical U-shaped conformation and is buried inside the central core of C-terminal α domain, similar to the conformation reported in other structures of cryptochromes and photolysases **(Figure 1c)**. Size exclusion and multi-angle-laser light scattering (SEC-MALLS) analyses suggest that *At*CRY2$_t$ in solution is bound to oxidized FAD as displayed by a yellow color, and mostly exists as monomers with relatively small fractions of oligomeric states **(Figure S2a-d)**. We were able to clearly identify the tetramer formation in solution under light conditions, yet we found that these oligomers tend to form large aggregates or photobodies and therefore failed to separate at significant UV-detectable levels **(Figure S2a-b)**, as reported in early studies of cryptochromes[19,21,33-35]. The crystallization process and nucleation events under light conditions appear to favor the tetrameric state. This is likely because the supersaturation event during vapor diffusion that results in high concentration of CRY2-FAD as exemplified by high intensity yellow

colored crystals **(Figure S2d)**. Overall, our *At*CRY2$_t$ structure is comparable with the recently reported low resolution CryoEM structure of *At*CRY2 and with the overall architecture of photo activated *Zm*CRY1C^{W368A} tetrameric structure[16].

Structure guided comparison analyses of *At*CRY2 reveals a photo-activated tetrameric state

The architecture within tetrameric *At*CRY2$_t$ is comprised of two different interfaces: a head to tail (H-T interface, monomers A-B) and head to head (H-H interface, monomers A-D) interaction between the monomers **(Figure 2a-b)**. Superposition of each of the individual monomers A-D reveals a similar overall structure with r.m.s. values ranging from 0.33 to 0.62 Å as measured for C$^{\alpha}$ atoms **(Figure S3a)**. In *At*CRY2$_t$, the interface (H-T) is assembled by the residues from α6, α12, α13, α18, α19, 3_{10}, L-24, L-26 **(Figure 2a)** and the second interface (H-H) is formed by the residues from α2, α10, α7 and L-11 **(Figure 2b)**. Analysis of the H-T interface reveals highly conserved residues that form salt-bridges and hydrogen bond interactions between the monomers **(Figure 2a** and **Figure S1)**. However, the H-H interface is stabilized by fewer ionic and hydrogen bonds interactions than the H-T **(Figure 2b)**. Structural superposition of *At*CRY2$_t$ with the photo-active mutant *Zm*CRY1C^{W368A} shows a similar structural arrangement yet an r.m.s deviation of 3.0 Å for 1368 residues **(Figure S3b)**. The superposition of a single monomer from each of these oligomeric structures shows an almost identical fold of the C$^{\alpha}$ atoms **(Figure S3c)**. The greater deviation when looking at the entirety of the tetramers is likely because of sequence variation between *Zea mays* CRY1 and *Arabidopsis thaliana* CRY2 and possibly a specific variation of oligomeric states. Further structural analysis revealed the presence of a unique 3_{10} helix in *At*CRY2$_t$ involved in the active H-T interface. This unique 3_{10} helix is present as a η-helix in active mutant of *Zm*CRY1C^{W368A} and in the monomeric *At*CRY2 **(Figure S3b** and **Figure S3e)**. Next

we compared *At*CRY2$_t$ structure to the recently reported *At*CRY2 monomeric structure (denoted *At*CRY2$_m$), and the *At*CRY2-BIC2 inhibitory complex (denoted *At*CRY2$_i$). Superposition of monomers A *vs*. D and B *vs*. C in the *At*CRY2$_t$ with the *At*CRY2$_m$ reveals no remarkable changes in the overall structure **(Figure S3d)**. However, superposition of monomers A and B of *At*CRY2$_t$ with the *At*CRY2$_m$ and its symmetry related molecule, shows that only monomer B of the tetramer is aligned with the monomer A of the symmetry related molecule (**Figure S3e**). This analysis strongly suggests that the H-H in *At*CRY2$_t$ is found to be similar to *At*CRY2$_m$ and *At*CRY2$_i$ structures, however H-T interface in *At*CRY2$_t$ is distinct during the active oligomeric state and can only be represented by symmetry related molecules in *At*CRY2$_m$ structure. Further comparison of the H-H interface shows fewer hydrogen bonds in *At*CRY2$_t$ compared to *At*CRY2$_m$ which forms 16 hydrogen bond interactions. This strongly suggests that larger conformational changes occur in the oligomerization process of *At*CRY2$_t$, which likely triggers movement in the subdomains that results in fewer interactions within the H-H interface. Also, *At*CRY2$_m$ and *Zm*CRY1C^{W368A} have three η-helices located in the H-T interface that are completely absent in *At*CRY2$_t$, suggesting more flexibility of the H-T interface within the tetrameric structure **(Figure S3e)**. This analysis further corroborates the recent findings that place the H-T interface as the initial interaction surface for BIC2, and substantiates this interface as a unique feature of active tetrameric structures[16,30,31,36]. Moreover, the structural comparison of *At*CRY2$_t$ with *At*CRY2$_m$ reveals approximately 54 structural alterations in amino acid side chain rotamers **(Figure S3f)**. Interestingly, most of these changes occur in highly conserved polar residues yet very few hydrophobic amino acids are altered. These differences are likely to play a role in salt bridges formation and stabilization of the active oligomeric state as was recently exemplified by mutational analysis[16,27]. One such change is the R439L mutation that leads to disruption of dimer interface formation both in vitro and *in*

vivo, and reduced binding of CIB1 peptide to the CRY2 photo-active H-T interface[16]. Altogether, these analyses substantiate yet again that *At*CRY2$_t$ represents a photo-activated tetramer and underlines the importance of H-T interface in photo-oligomerization.

The dynamic role of *At*CRY2$_t$ connecting loop in photo-oligomerization

To further characterize CRYs structural conformations and photo-oligomerization states, we carried out structure-guided comparative analysis of active and inactive CRYs. We uncovered a dynamic highly conserved interconnecting loop that wraps around the α/β domain. In *At*CRY2$_t$ this connecting loop has two defined helices (α5 and α6) but it is largely disordered **(Figure 3a** and **Figure S1)**. As expected for active states, the conformation of the connecting loop within *At*CRY2$_t$ is found to be relatively similar to the *Zm*CRY1C^{W368A} **(Figure 3b)**, suggesting a unique structural feature of photo activated CRYs. Remarkably, comparative characterization of non-oligomeric CRYs, reveals significant structural deviation between active and inactive states. We identified multiple secondary structure differences centered in 3_{10} helix and short α-helices (residues 144-146, 181-184, 187-190, and 189-192, **Figure 3c**). These structural variances strongly suggest a large movement of the N and C domains between the active and inactive states of CRYs **(Figure 3c** and **Movie S1)**. Despite the sequence conservation in the connecting loop, superposition of the residues 163-190 in *At*CRY2$_m$ demonstrates major side chain alterations compared to *At*CRY2$_t$ **(Figure 3d-e)**. These changes can be explained by the inherent flexibility of the unstructured coiled coil and the overall active and inactive conformational states of CRYs (**Movie S2**). Notably, the disulfide bond C80-C190 in *At*CRY1 between the α/β domain and the connector region is not found in *At*CRY2, wherein the non-conserved residue C80 is replaced with D73 (**Figure 3e** and **S1**). Our data suggest that the absence of secondary structural elements in

active CRYs significantly increases the plasticity and the movement of α6 helix to actively participate in the interface formation. Furthermore, the connecting loop contains multiple residues that were already shown to be implicated in the photo-activated oligomer interface such as R208, N203, and S202. This further validates the flexibility of the connecting loop and places it as one of the central structural elements that regulates the photo-oligomeric state.

Structural insights into inhibition of CRYs oligomerization by BICs

To further delineate the mode of BIC2 prevention of CRY2 oligomerization, we examined the structural changes between active *At*CRY2$_t$ and *At*CRY2$_i$ (inhibitory CRY2-BIC2 complex)[32]. The H-T interface in *At*CRY2$_t$ is formed by L-26 on one side of the monomer and α18 on the other side **(Figure 4a-b)**. In *At*CRY2$_i$ the α1 helix of BIC2 is inserted straight in the middle of the H-T interface and clearly clashes with the residues in α18, α19 and L-26, thus preventing or disrupting the oligomerization of *At*CRY2 **(Figure 4b)**. Specifically, within *At*CRY2$_t$ H-T interface, the residue R208 (monomer A) forms ionic interactions with E428 (monomer B). Similarly, Q333 residue (monomer A) forms ionic interactions with E462 (monomer B), and bifurcated hydrogen bond interactions with T465 and N466 (monomer B). These interactions are completely disrupted upon BIC binding, where the residues E50 and D59 of BIC2 form ionic interactions with R208 and Q333 **(Figure 4b-c** and **Figure 3)**. Here, the *At*CRY2$_t$ tetrameric structure provides a unique opportunity to inspect the specific mode of BIC2 oligomeric disruption. Our structural analysis corroborates certain residues involved in the CRY2-BIC2 interface as suggested previously[32], but also reveals new key residues such as E462, T465 and N466 that play critical roles in oligomerization and BIC2 mechanism of inhibition.

Comparative analysis of FAD binding pocket of photo activated CRYs

Given the critical role of FAD in photoreduction process, we used the *At*CRY2$_t$ tetrameric structure to provide a detailed analysis of FAD binding cavity in photo-activated state. The FAD binding pocket within *At*CRY2$_t$ occupies a larger surface area of 849.6 Å^2 compared to *At*CRY2$_m$ which occupies a surface area of 821 Å^2. The FAD access cavity is comprised of positively charged residues that stabilize the negatively rich phosphate moiety of FAD **(Figure 5a)**. The adenine and isoalloxazine ring of FAD are stabilized by polar and negatively charged residues that form the core region of the FAD pocket **(Figure 5b)**. The flexible phosphate moiety of FAD is held in place by forming hydrogen bonds with the backbone and side chains atoms of the residues T244, S245, L246, S248, W353, R359, D387 and D389. The isoalloxazine and adenine di-nucleotide ring position parallel to each other and each ring is stabilized by interactions with nearby amino acid residues (such as N356, R359, D387, D389 and D393). This extensive hydrogen bond network substantially supports the U-shaped conformation of FAD (**Figure 5b** and **Figure S4a-b**). A striking feature of photolyases and plant cytochromes is the substitution of the amino acid N380 to D393 [24,37,38], which is a highly conserved key position within the FAD binding pocket (**Figure 5c** and **Figure S4c)**. This residue plays a significant role in determining the redox property of FAD by acting as an acid or base and carries a net negative charge that destabilizes FADH$^-$ [24]. It has been shown that D393A mutant exhibit loss in the photoreduction activity[32]. Similarly, a mutant in *At*CRY1 of D396C leads to a complete loss or block of proton transfer to the N5 atom of Flavin[39]. Interestingly, a comparison between plant CRY1 and CRY2 identified a key conserved change of D359 (CRY1s) to N356 in CRY2s; this conserved change is similarly found in other photolyases (**Figure 5c, Figure S1** and **Figure S4d**). In CRY1, D359 forms a strong hydrogen bond interaction with the oxygen atom of FAD, however in *At*CRY2$_t$, N356 only forms electrostatic interactions. This may explain the reported differences in light sensing mechanisms

between CRY1 and CRY2 [11,40]. Comparative structural analysis of the FAD cavity between *At*CRY2$_t$ and *At*CRY2$_m$ shows almost no variations in the side chains (**Figure S4b**). However, when comparing between *At*CRY2$_t$ and *At*CRY2$_i$, we detected a significant 180° conversion within the FAD atom orientations centered in O3 and O4 (**Figure S4c**). It is yet unclear how exactly this change contributes to the understanding of CRY2-BICs inhibitory complex. Altogether, the absence of major deviations within the FAD binding pocket suggests that FAD cavity does not play a direct role in triggering conformational changes during oligomerization. Nonetheless, the distance between D393 and FAD in inactive CRYs (e.g., *At*CRY2$_i$) shows a larger difference compared to the active oligomeric structures **(**e.g., *At*CRY2$_t$, **Figure 5d)**. This suggests that electron transfer related residues may undergo conformational changes during oligomerization and indirectly affect the FAD redox state.

_At_CRY2$_t$ crystal structure captures an intermediate electron transfer *via* Trp-triad and implies conformational changes between active and inactive states

To better understand the role of Trp-triad and electron transfer in photo-oligomeric states, we next carried out a systematic structural inspection of all reported CRYs atomic models including *At*CRY2$_t$ reported in this study. It has been previously suggested that the distances between tryptophan residues play an imperative role in the photocycle of cryptochromes and determine their active state in vitro [17,41]. In the crystal structure of *At*CRY2$_t$, the three key tryptophan residues: distal W321, central W374, and FAD-proximal W397 are found in atomic resolution and aligned with the overall arrangement of the canonical Trp-triad **(Figure S4e)**. Our comparative analysis found only subtle structural variation in the FAD-proximal tryptophan W397 of *At*CRY2$_t$, *At*CRY2$_m$ and *At*CRY2$_i$. However, significant distance deviations were measured between central

W374 and distal W321 of *At*CRY2$_t$ and found to be greater (6.5Å) compared to the distance measured for *At*CRY2$_m$ (4.9Å), AtCRY2$_i$ (4.8Å), and *At*CRY1 (5.9Å) **(Figure 5d)**. Interestingly, the distances between W374-W397 and W397-D393 are found to be shorter in *At*CRY2$_t$ (4.5Å and 3Å) and greater in *At*CRY2$_m$ (6.7Å and 3.4Å), *At*CRY2$_i$ (6Å and 3.8Å), *At*CRY1 (5.3Å and 3.3Å), and *Zm*CRY1C (7.6Å and 4.5Å) **(Figure 5d** and **Figure S4e)**. The greater distances observed in *At*CRY2$_m$, *At*CRY2$_i$, and *Zm*CRY1C^{W368A} from the FAD and within the Trp triad, indicate that the conformation adopted by tryptophan may not be suitable for efficient electron transfer in the inactive state. Altogether these results suggest that the Trp triad is re-arranged upon exposure to blue-light to carry out active photoreduction process. Further analyses show that in *At*CRY2$_m$ and *At*CRY2$_i$ the distance between the D393 and N5 of isoalloxazine ring of FAD (O-H^{D393}…N5^{ISO}) complex is close (3.0Å); unlike the active oligomeric structures *At*CRY2$_t$ and *Zm*CRY1C^{W368A} where the distance between the D393 and N5 of isoalloxazine is measured to be farther (3.8Å) **(Figure 5d)**. This is likely because in the active oligomeric state, D393 appeared to be oriented towards W397 via hydrogen bonds. In comparison to monomeric CRYs, *At*CRY2$_t$ exhibits the largest distance between W321-W374 and the least distance between W374-W397 and W397-D393. This finding strongly suggests that *At*CRY2$_t$ is in a suitable active conformation for efficient electron transfer during photoreduction process. Altogether, our structure-based distance examination of the Trp triad and D393-W397 suggests that the crystal structure of *At*CRY2$_t$ has been trapped in a light-activated intermediate state where the D393 accepts an electron from N1 of W397 **(Figure 5d** and **Figure S4e)**.

Discussion

Since the discovery of plant CRYs, an increasing number of studies have provided important insights that link light-induced photoreduction and activation of CRYs by homo-oligomerization[27,28,42]. The reported structure of mutant maize CRY1 (*Zm*CRY1C^{W368A}) validates these functional studies by providing the photo-activated oligomeric states of CRYs[16]. Additionally, the crystal structure of the Arabidopsis inhibitory BIC2-CRY2 complex illuminated the mechanism of inactivation of monomeric CRYs[32]. These studies advance our knowledge of photo-responsive events between activated CRYs and their desensitization upon binding with the dynamic regulatory inhibitor BICs. Nonetheless, our understanding of CRYs light signaling mechanism, structural aspects for their activation, and oligomerization, remained to be fully addressed. The tetrameric structure of CRY2 had not been resolved in high resolution and a detailed structural analysis that links between photo-oligomerization and BICs inhibition had yet to be performed. In this work, we report the active tetrameric crystal structure of the *At*CRY2$_t$ PHR domain. To our knowledge this is the first native, high-resolution crystal structure of tetrameric CRY2. We identified two distinct interfaces H-H and H-T that play critical roles in light induced conformational changes. Our structural analysis dissects the active interface (H-T) that is disrupted when BIC2 is bound. BIC2 represents a family of key transcriptional regulators including BIC1 and CIB1, therefore our proposed model of oligomeric inhibition as well as the residues involved are likely to be similar for other CRYs inhibitory complexes. Detailed structure-based analyses using the structure of *At*CRY2$_t$ allowed us to corroborate the recently reported CRY2 and CRY1 structures, but also to reveal novel residues (such as E462, N466, and T465) that are involved in CRYs oligomerization. Our findings reveal remarkable changes in approximately 54 amino acids orientations between the photo-active and inactive states of CRY2, suggesting that CRY2

undergoes conformational changes upon photoactivation. This study further elucidates a large evolutionarily conserved interconnecting loop (residues 133-213) that exhibits dynamic conformational changes between the active and inactive CRYs states. Several residues within the connecting loop were found to be directly implicated in photo-oligomerization (such as R208, S202, N203), and certain regions (such as α6) were found to be more adaptable to the tetrameric state. Interestingly, the structural changes in the secondary structures between the active and inactive CRYs that are centered in the connecting loop suggest further molecular regulations. In fact, recent *in vivo* studies of photoexcited Arabidopsis CRY2 identified four key residues (T149, S162, T178, and S188) that undergo phosphorylation upon photoexcitation[43]. Notably, these residues are positioned within the dynamic short helices of CRYs (T178, S188) or in close proximity to them, although defining the role of CRYs connecting loop in light-induced regulations awaits further studies.

The importance of the Trp-triad in CRYs and their convoluted role in photo-signaling has been addressed in many studies and has been a subject of debate in the field. We address the role of the Trp-triad by analyzing the structures of oligomeric active and monomeric inactive CRYs. Interestingly, within the Trp-triad we found distinct intra-residue distances between inactive and photoactive CRYs. Our detailed structure-based analysis suggests that the tryptophan residues likely adopt various structural re-arrangements that dictate the efficiency of electron transfer based on CRYs inactive or photoactive state. The calculated distances suggest that the oligomeric active CRY2 structure is likely recapitulating an activated intermediate electron transfer state between the FAD and D393-W397. This finding substantiates a number of mutational analysis studies that highlight the importance of these residues in preserving the redox potential and stabilization of the FAD radical[25,44].

Based on our current understanding including the crystal structure reported here, we propose the following model of CRY-mediated blue light induced photoreduction in plants **(Figure 6)**. Under dark conditions, CRYs are likely to exist as monomers, wherein the PHR domain is bound with the CCE domain. Upon exposure to blue light, the FAD molecule (within the PHR) absorbs energy and accepts electrons through the Trp triad photoreduction pathway. This would subsequently cause a structural rearrangement including the disassociation of the CCE domain from the PHR[10,45,46]. The photoexcited PHR domain then undergoes homo-oligomerization that involves multiple structural rearrangements including the major conformational changes we observed in the interconnecting loop. These active oligomers are subsequently regulated by numerous downstream biological processes that are responsible for the plant physiological response. By leveraging the reported CRYs structure with our active tetrameric CRY2, we were able to provide a comprehensive molecular view into BICs direct mode of inhibition. Whether BICs compete off the H-T interface or completely prevent oligomerization remains to be elucidated *in vivo*. In summary, our study further extends the understanding of plant photo-sensing molecular mechanisms by revealing and analyzing the distinct structural changes between photoactive tetrameric and inactive monomeric states of cryptochromes.

Methods

Protein preparation and purification

The CRY2-PHR (*Arabidopsis thaliana*, 1-498) was cloned into pFastbac-GST vector and expressed as a GST fusion protein in Hi5 suspension insect cells. CRY2-PHR was isolated from the soluble cell lysate by glutathione sepharose (GE Healthcare) using a buffer containing 50 mM Tris-HCl, pH 7.5, 200 mM NaCl, 4% Glycerol, 5 mM DTT. Proteins were further purified *via* on-column cleavage by TEV protease, followed by cation exchange and size exclusion chromatography. Protein was concentrated by ultrafiltration to 3–10 mg/mL^{-1}. Purified CRY2-PHR was eluted off a Superdex-200 gel filtration column (GE healthcare) in 20 mM Tris, pH 8.0, 200 mM NaCl, 2 mM DTT, 4% Glycerol. *At*CRY2-PHR protein existed mainly as monomer with an estimated molecular weight of 55kDa, dimers and tetramers only accounted for a small portion of gel filtration elutions.

Crystallization, data collection and structure determination

The crystals of *At*CRY2-PHR were grown at 25 °C by the hanging-drop vapor diffusion method with 1.0 µL protein complex sample mixed with an equal volume of reservoir solution containing 1.5M Sodium Nitrate; 0.1M BIS-TRIS propane pH 7.0. Crystals of maximum size were obtained and harvested after 2 weeks. The crystals were harvested from the reservoir solution with additional final concentration of 20% glycerol serving as cryoprotectant. X-ray diffraction data were integrated and scaled with HKL2000 package[47]. The CRY2-PHR structure was determined by molecular replacement using the *At*CRY1 structure (PDB: 1U3C)[48] as the search model. The structure model was manually built, refined, and rebuilt with PHENIX[49] and COOT[50].

Size exclusion chromatography and multi-angle-laser light scattering (MALS) analysis

Purified proteins (20-50 μM) were injected onto Superdex-200 Increase 10/300 column (GE Healthcare) for analysis at a flow rate of 0.5 mL min^{-1}. The elution fractions (0.5 ml/fraction) were resolved by SDS-PAGE and analyzed by Coomassie Brilliant Blue G-250 stain. Molecular weights were estimated by comparison to known standards (Bio-Rad). For SEC-MALS analysis, Superdex-200 Increase 10/300 column was equilibrated with 50mM HEPES pH 7.0, 120mM KCl buffer (filtered through 0.22 μm filter and sonicated), recirculated through the system overnight at 0.5 mL mL min^{-1}. 100 μL of protein solution (2-3 mg mL^{-1}) was injected, and the data from detectors was exported at room temperature. All experiments were repeated thrice. Data was analyzed with ASTRA software package version 5.3.2.10 (Wyatt Technologies).

UV-Vis protein absorption spectra

Purified AtCRY2-PHR (2-3 mg mL^{-1}) absorption spectrum was measured on a NanoDrop One Microvolume UV-Vis Spectrophotometer from 300-700 nm every 10 nm in triplicate under room light conditions and averaged. Arbitrary absorption units (a.u.) were normalized against a blank buffer without protein.

***In silico* sequence and structural analyses**

Representative cryptochrome sequences were gathered from NCBI protein database. Amino acid alignments were performed with CLC Genomics Workbench v12 using a slow progressive alignment algorithm. Photolyase sequence is included as an outgroup to plant cryptochromes.

The surface area of FAD binding pocket is analyzed using PDBePISA online tool[26]. For electrostatic charge distribution, the Adaptive Poisson-Boltzmann Solver (APBS) program[51]

implemented in PyMOL was employed to calculate the electrostatic charge distribution of *At*CRY2$_t$. All the figures in this manuscript was made using PyMOL. The LigPlot program[52] was used for 2-D representation of protein-ligand interactions in standard PDB data format.

Data Availability

The atomic coordinates of *At*CRY2-PHR structure has been deposited in the Protein Data Bank with accession codes 6X24.

Acknowledgements

We thank the beamline staff at ALS for help with data collection, Ning Zheng and Jawdat Al-Bassam for discussion and help. This work is supported by UC Davis new faculty start-up funds.

Author Contributions

N.S., M.P., J.G. conceived and designed the experiments. N.S. and S.D. conducted the protein purification and crystallization experiments. N.S, M.P., and determined and analyzed the structures. N.S., and S.D. conceived and conducted the SEC experiments and help with sample preparation. M.P., J.G., and A.G. conducted in silico studies and analyses. N.S., M.P., J.G., A.G., and L.T., wrote the manuscript with the help from all other co-authors.

Author Information

Authors declare no competing interests. Correspondence and requests for materials should be addressed to N.S. (nshabek@ucdavis.edu).

References

1 Canamero, R. C. *et al.* Cryptochrome photoreceptors cry1 and cry2 antagonistically regulate primary root elongation in Arabidopsis thaliana. *Planta* **224**, 995-1003, doi:10.1007/s00425-006-0280-6 (2006).

2 Kang, C. Y., Lian, H. L., Wang, F. F., Huang, J. R. & Yang, H. Q. Cryptochromes, phytochromes, and COP1 regulate light-controlled stomatal development in Arabidopsis. *Plant Cell* **21**, 2624-2641, doi:10.1105/tpc.109.069765 (2009).

3 Xu, P. *et al.* Wheat cryptochromes: subcellular localization and involvement in photomorphogenesis and osmotic stress responses. *Plant Physiol* **149**, 760-774, doi:10.1104/pp.108.132217 (2009).

4 Weller, J. L. *et al.* Genetic dissection of blue-light sensing in tomato using mutants deficient in cryptochrome 1 and phytochromes A, B1 and B2. *Plant J* **25**, 427-440, doi:10.1046/j.1365-313x.2001.00978.x (2001).

5 Guo, H., Yang, H., Mockler, T. C. & Lin, C. Regulation of flowering time by Arabidopsis photoreceptors. *Science* **279**, 1360-1363, doi:10.1126/science.279.5355.1360 (1998).

6 Kleine, T., Lockhart, P. & Batschauer, A. An Arabidopsis protein closely related to Synechocystis cryptochrome is targeted to organelles. *Plant J* **35**, 93-103, doi:10.1046/j.1365-313x.2003.01787.x (2003).

7 Ahmad, M. & Cashmore, A. R. HY4 gene of A. thaliana encodes a protein with characteristics of a blue-light photoreceptor. *Nature* **366**, 162-166, doi:10.1038/366162a0 (1993).

8 Khan, S. K. *et al.* Identification of a novel cryptochrome differentiating domain required for feedback repression in circadian clock function. *J Biol Chem* **287**, 25917-25926, doi:10.1074/jbc.M112.368001 (2012).

9 Yu, X., Liu, H., Klejnot, J. & Lin, C. The Cryptochrome Blue Light Receptors. *Arabidopsis Book* **8**, e0135, doi:10.1199/tab.0135 (2010).

10 Liu, B. *et al.* Signaling mechanisms of plant cryptochromes in Arabidopsis thaliana. *J Plant Res* **129**, 137-148, doi:10.1007/s10265-015-0782-z (2016).

11 Lin, C. *et al.* Association of flavin adenine dinucleotide with the Arabidopsis blue light receptor CRY1. *Science* **269**, 968-970, doi:10.1126/science.7638620 (1995).

12 Malhotra, K., Kim, S. T., Batschauer, A., Dawut, L. & Sancar, A. Putative blue-light photoreceptors from Arabidopsis thaliana and Sinapis alba with a high degree of sequence homology to DNA photolyase contain the two photolyase cofactors but lack DNA repair activity. *Biochemistry* **34**, 6892-6899, doi:10.1021/bi00020a037 (1995).

13 Banerjee, R. *et al.* The signaling state of Arabidopsis cryptochrome 2 contains flavin semiquinone. *J Biol Chem* **282**, 14916-14922, doi:10.1074/jbc.M700616200 (2007).

14 Hoang, N., Bouly, J. P. & Ahmad, M. Evidence of a light-sensing role for folate in Arabidopsis cryptochrome blue-light receptors. *Mol Plant* **1**, 68-74, doi:10.1093/mp/ssm008 (2008).

15 Bouly, J. P. *et al.* Cryptochrome blue light photoreceptors are activated through interconversion of flavin redox states. *J Biol Chem* **282**, 9383-9391, doi:10.1074/jbc.M609842200 (2007).

16 Shao, K. *et al.* The oligomeric structures of plant cryptochromes. *Nat Struct Mol Biol* **27**, 480-488, doi:10.1038/s41594-020-0420-x (2020).

17 Partch, C. L. & Sancar, A. Photochemistry and photobiology of cryptochrome blue-light photopigments: the search for a photocycle. *Photochem Photobiol* **81**, 1291-1304, doi:10.1562/2005-07-08-IR-607 (2005).

18 Yang, H. Q., Tang, R. H. & Cashmore, A. R. The signaling mechanism of Arabidopsis CRY1 involves direct interaction with COP1. *Plant Cell* **13**, 2573-2587, doi:10.1105/tpc.010367 (2001).

19 Wang, H., Ma, L. G., Li, J. M., Zhao, H. Y. & Deng, X. W. Direct interaction of Arabidopsis cryptochromes with COP1 in light control development. *Science* **294**, 154-158, doi:10.1126/science.1063630 (2001).

20 Li, X. *et al.* Arabidopsis cryptochrome 2 (CRY2) functions by the photoactivation mechanism distinct from the tryptophan (trp) triad-dependent photoreduction. *Proc Natl Acad Sci U S A* **108**, 20844-20849, doi:10.1073/pnas.1114579108 (2011).

21 Wang, Q. & Lin, C. A structural view of plant CRY2 photoactivation and inactivation. *Nat Struct Mol Biol* **27**, 401-403, doi:10.1038/s41594-020-0432-6 (2020).

22 Giovani, B., Byrdin, M., Ahmad, M. & Brettel, K. Light-induced electron transfer in a cryptochrome blue-light photoreceptor. *Nat Struct Biol* **10**, 489-490, doi:10.1038/nsb933 (2003).

23 Byrdin, M., Eker, A. P., Vos, M. H. & Brettel, K. Dissection of the triple tryptophan electron transfer chain in Escherichia coli DNA photolyase: Trp382 is the primary donor in photoactivation. *Proc Natl Acad Sci U S A* **100**, 8676-8681, doi:10.1073/pnas.1531645100 (2003).

24 Scheerer, P. *et al.* The class III cyclobutane pyrimidine dimer photolyase structure reveals a new antenna chromophore binding site and alternative photoreduction pathways. *J Biol Chem* **290**, 11504-11514, doi:10.1074/jbc.M115.637868 (2015).

25 Liu, B., Liu, H., Zhong, D. & Lin, C. Searching for a photocycle of the cryptochrome photoreceptors. *Curr Opin Plant Biol* **13**, 578-586, doi:10.1016/j.pbi.2010.09.005 (2010).

26 Krissinel, E. & Henrick, K. Inference of macromolecular assemblies from crystalline state. *J Mol Biol* **372**, 774-797, doi:10.1016/j.jmb.2007.05.022 (2007).

27 Liu, Q. *et al.* Photooligomerization Determines Photosensitivity and Photoreactivity of Plant Cryptochromes. *Mol Plant* **13**, 398-413, doi:10.1016/j.molp.2020.01.002 (2020).

28 Wang, Q. & Lin, C. Mechanisms of Cryptochrome-Mediated Photoresponses in Plants. *Annu Rev Plant Biol* **71**, 103-129, doi:10.1146/annurev-arplant-050718-100300 (2020).

29 Wang, Q. *et al.* Beyond the photocycle-how cryptochromes regulate photoresponses in plants? *Curr Opin Plant Biol* **45**, 120-126, doi:10.1016/j.pbi.2018.05.014 (2018).

30 Wang, X. *et al.* A CRY-BIC negative-feedback circuitry regulating blue light sensitivity of Arabidopsis. *Plant J* **92**, 426-436, doi:10.1111/tpj.13664 (2017).

31 Liu, H. *et al.* Photoexcited CRY2 interacts with CIB1 to regulate transcription and floral initiation in Arabidopsis. *Science* **322**, 1535-1539, doi:10.1126/science.1163927 (2008).

32 Ma, L. *et al.* Structural insights into BIC-mediated inactivation of Arabidopsis cryptochrome 2. *Nat Struct Mol Biol* **27**, 472-479, doi:10.1038/s41594-020-0410-z (2020).

33 Ozkan-Dagliyan, I. *et al.* Formation of Arabidopsis Cryptochrome 2 photobodies in mammalian nuclei: application as an optogenetic DNA damage checkpoint switch. *J Biol Chem* **288**, 23244-23251, doi:10.1074/jbc.M113.493361 (2013).

34 Mas, P., Devlin, P. F., Panda, S. & Kay, S. A. Functional interaction of phytochrome B and cryptochrome 2. *Nature* **408**, 207-211, doi:10.1038/35041583 (2000).

35 Yu, X. *et al.* Formation of nuclear bodies of Arabidopsis CRY2 in response to blue light is associated with its blue light-dependent degradation. *Plant Cell* **21**, 118-130, doi:10.1105/tpc.108.061663 (2009).

36 Wang, Q. *et al.* Photoactivation and inactivation of Arabidopsis cryptochrome 2. *Science* **354**, 343-347, doi:10.1126/science.aaf9030 (2016).

37 Mei, Q. & Dvornyk, V. Evolutionary History of the Photolyase/Cryptochrome Superfamily in Eukaryotes. *PLoS One* **10**, e0135940, doi:10.1371/journal.pone.0135940 (2015).

38 Xu, L. & Zhu, G. The Roles of Several Residues of Escherichia coli DNA Photolyase in the Highly Efficient Photo-Repair of Cyclobutane Pyrimidine Dimers. *J Nucleic Acids* **2010**, doi:10.4061/2010/794782 (2010).

39 Hense, A., Herman, E., Oldemeyer, S. & Kottke, T. Proton transfer to flavin stabilizes the signaling state of the blue light receptor plant cryptochrome. *J Biol Chem* **290**, 1743-1751, doi:10.1074/jbc.M114.606327 (2015).

40 Lin, C., Ahmad, M., Gordon, D. & Cashmore, A. R. Expression of an Arabidopsis cryptochrome gene in transgenic tobacco results in hypersensitivity to blue, UV-A, and green light. *Proc Natl Acad Sci U S A* **92**, 8423-8427, doi:10.1073/pnas.92.18.8423 (1995).

41 Kimo, S. M., Friis, I. & Solov'yov, I. A. Atomistic Insights into Cryptochrome Interprotein Interactions. *Biophys J* **115**, 616-628, doi:10.1016/j.bpj.2018.06.029 (2018).

42 Hallett, R. A., Zimmerman, S. P., Yumerefendi, H., Bear, J. E. & Kuhlman, B. Correlating in Vitro and in Vivo Activities of Light-Inducible Dimers: A Cellular Optogenetics Guide. *ACS Synth Biol* **5**, 53-64, doi:10.1021/acssynbio.5b00119 (2016).

43 Liu, Q. *et al.* Molecular basis for blue light-dependent phosphorylation of Arabidopsis cryptochrome 2. *Nat Commun* **8**, 15234, doi:10.1038/ncomms15234 (2017).

44 Thoing, C., Oldemeyer, S. & Kottke, T. Microsecond Deprotonation of Aspartic Acid and Response of the alpha/beta Subdomain Precede C-Terminal Signaling in the Blue Light Sensor Plant Cryptochrome. *J Am Chem Soc* **137**, 5990-5999, doi:10.1021/jacs.5b01404 (2015).

45 Kondoh, M. *et al.* Light-induced conformational changes in full-length Arabidopsis thaliana cryptochrome. *J Mol Biol* **413**, 128-137, doi:10.1016/j.jmb.2011.08.031 (2011).

46 Wang, Q. *et al.* The Blue Light-Dependent Phosphorylation of the CCE Domain Determines the Photosensitivity of Arabidopsis CRY2. *Mol Plant* **10**, 357, doi:10.1016/j.molp.2016.12.009 (2017).

47 Otwinowski, Z. & Minor, W. Processing of X-ray diffraction data collected in oscillation mode. *Methods Enzymol* **276**, 307-326 (1997).

48 Brautigam, C. A. *et al.* Structure of the photolyase-like domain of cryptochrome 1 from Arabidopsis thaliana. *Proc Natl Acad Sci U S A* **101**, 12142-12147, doi:10.1073/pnas.0404851101 (2004).

49 Afonine, P. V. *et al.* Real-space refinement in PHENIX for cryo-EM and crystallography. *Acta Crystallogr D Struct Biol* **74**, 531-544, doi:10.1107/S2059798318006551 (2018).

50 Emsley, P. & Cowtan, K. Coot: model-building tools for molecular graphics. *Acta Crystallogr D Biol Crystallogr* **60**, 2126-2132, doi:10.1107/S0907444904019158 (2004).

51 Jurrus, E. *et al.* Improvements to the APBS biomolecular solvation software suite. *Protein Sci* **27**, 112-128, doi:10.1002/pro.3280 (2018).

52 Wallace, A. C., Laskowski, R. A. & Thornton, J. M. LIGPLOT: a program to generate schematic diagrams of protein-ligand interactions. *Protein Eng* **8**, 127-134, doi:10.1093/protein/8.2.127 (1995).

53 Park, H. W., Kim, S. T., Sancar, A. & Deisenhofer, J. Crystal structure of DNA photolyase from Escherichia coli. *Science* **268**, 1866-1872, doi:10.1126/science.7604260 (1995).

54 Mees, A. *et al.* Crystal structure of a photolyase bound to a CPD-like DNA lesion after in situ repair. *Science* **306**, 1789-1793, doi:10.1126/science.1101598 (2004).

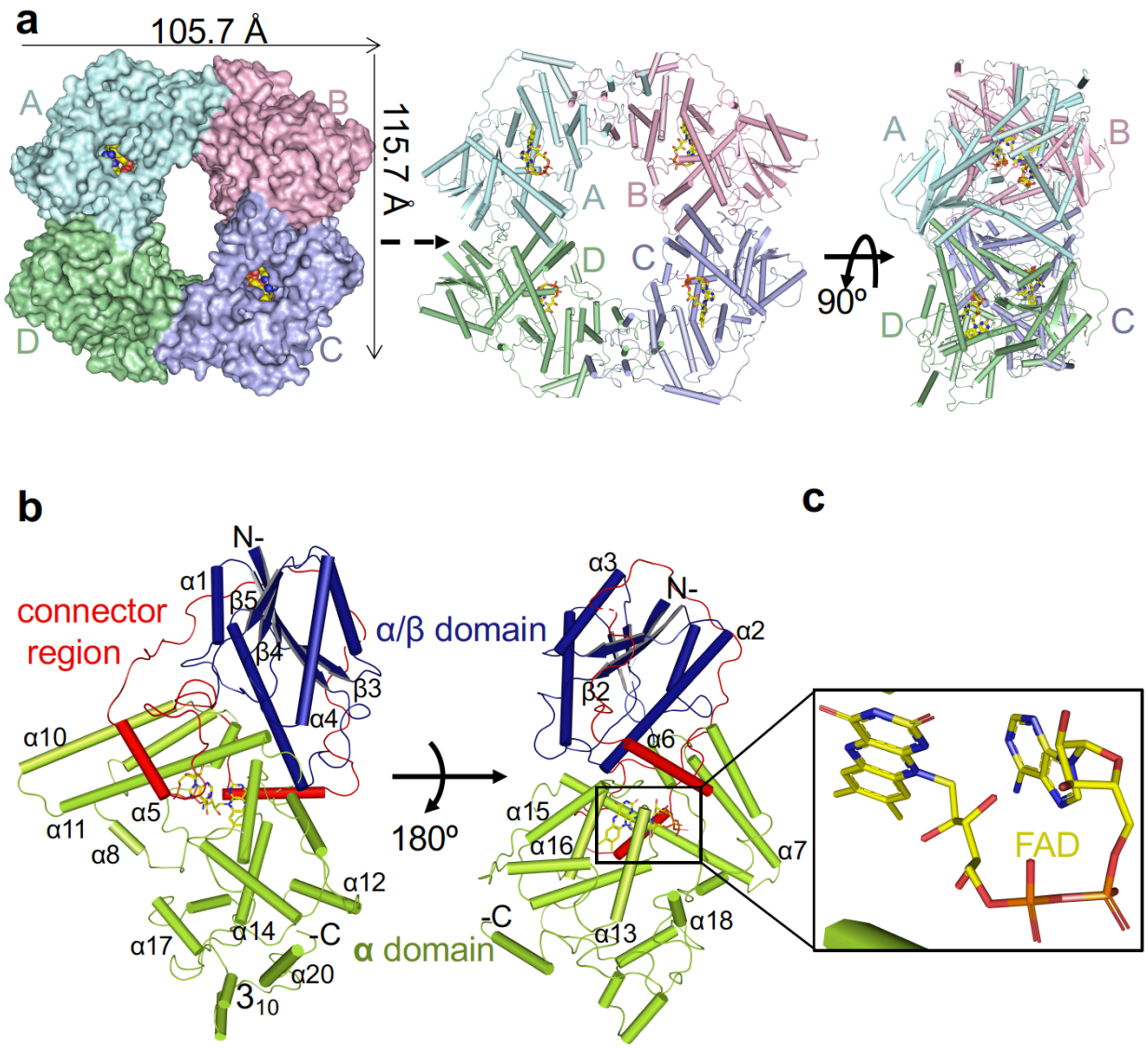

Figure 1. Molecular architecture of CRY2. (a) Overall structure of CRY2 bound to FAD shown in top view surface representation (left), cylinders (middle), and side view (right) with the four monomers A-D assembled to a tetramer (A,B,C,D represented by cyan, pink, purple, and green respectively). FAD molecules are shown in yellow. **(b)** Close-up view of *At*CRY2$_t$ monomer represented in cartoon. Secondary structure of the indicated domains shown as cylinders for helices and beta strands and labeled in black. N-terminal α/β domain (blue), C-terminal α-domain (green), and flexible connector loop (in red) are highlighted. **(c)** Close-up view of bound FAD represented in sticks and colored by elements: yellow (carbon), blue (nitrogen), red (oxygen), phosphate (orange).

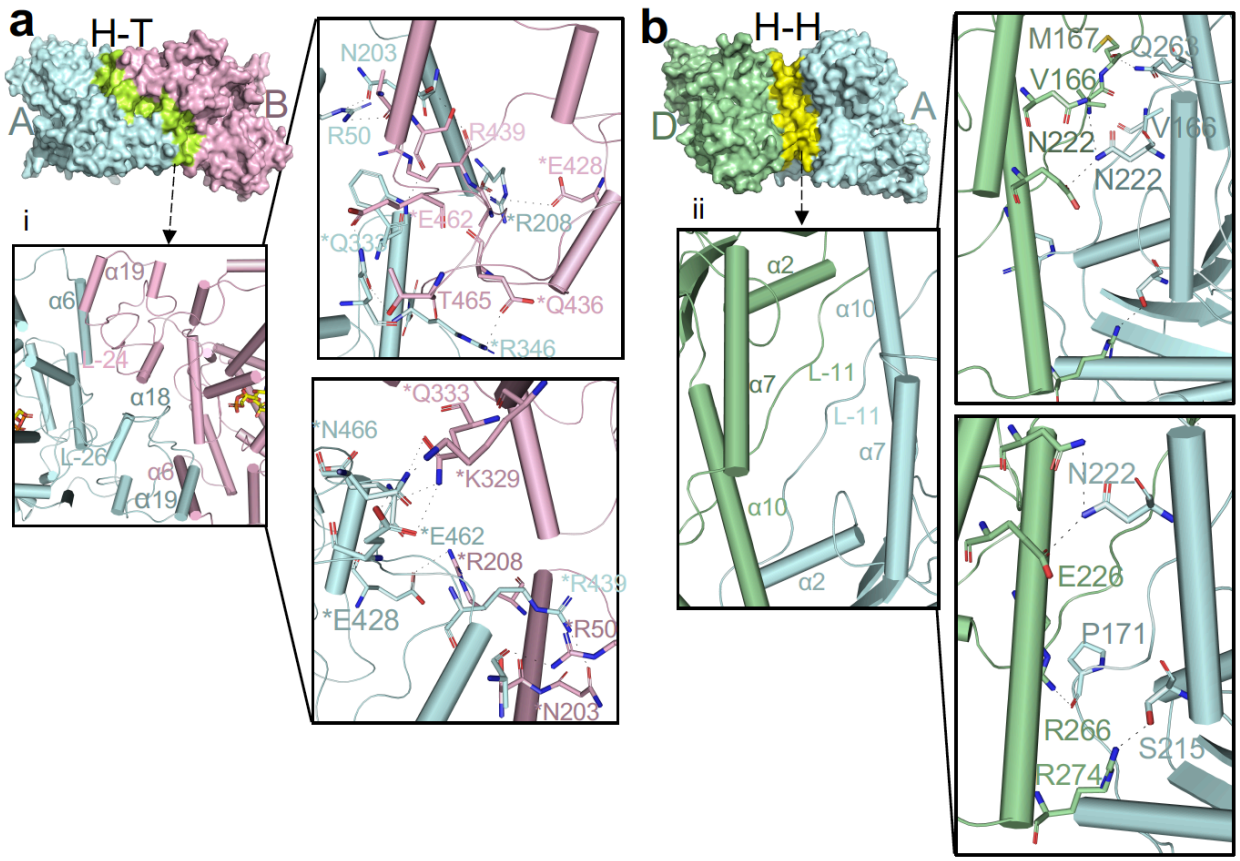

Figure 2. Oligomeric interfaces of CRY2. (a) *Upper left*, side view surface representation of head to tail (H-T) interface (green) of A and B monomers (cyan and pink respectively); (i) Close-up views of H-T interface indicated by helices positions and all the amino acids that form direct interactions (*upper right and lower right panel*). Asterisks represent residues that form salt-bridges **(b)** *Upper right*, side view surface representation of head to head (H-H) interface (yellow) of A and D monomers (cyan and green respectively); (ii) Close-up of H-H interface indicated by helices positions and all the amino acids that form direct interactions (*upper right panel and lower left panel*).

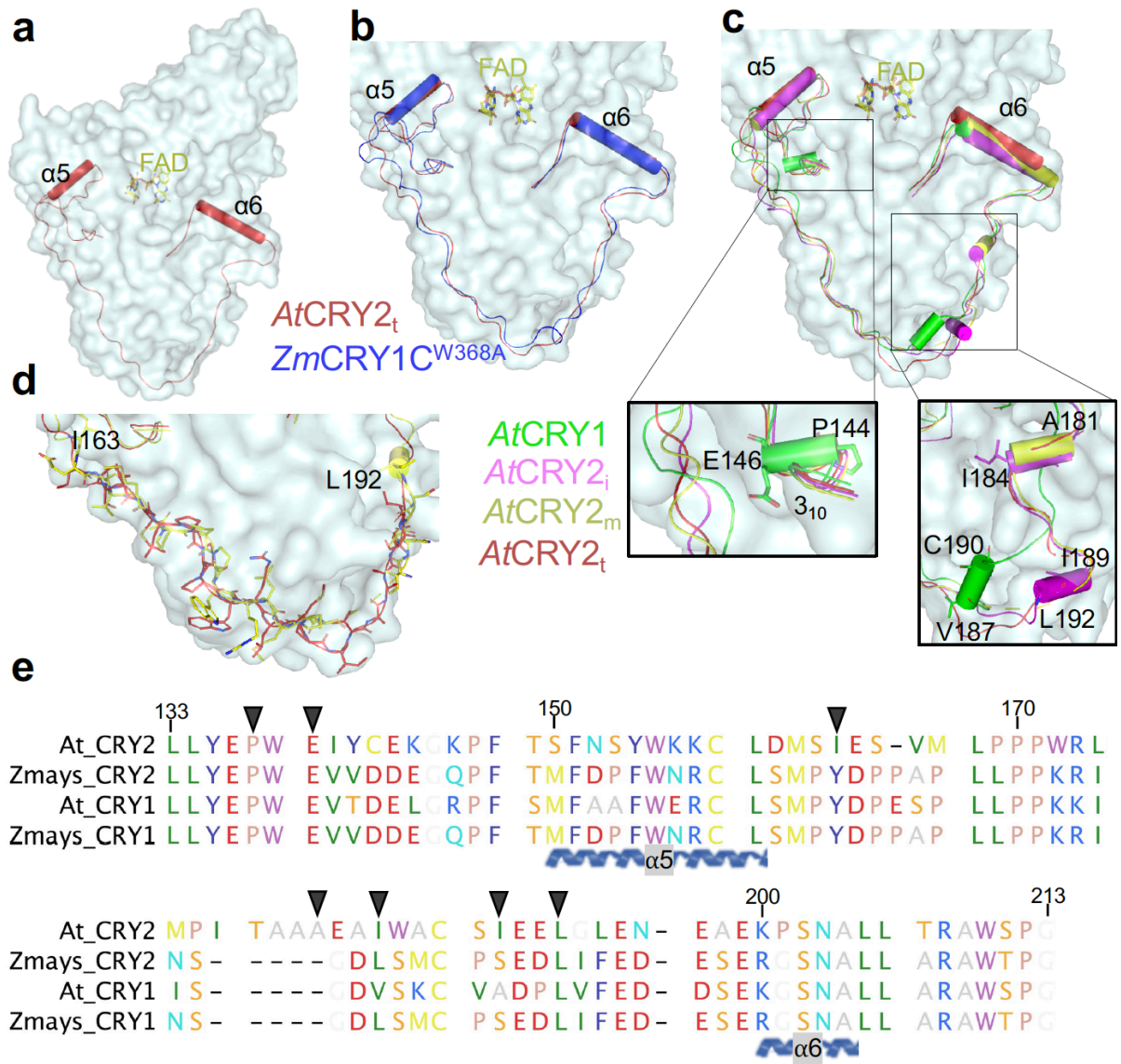

Figure 3. Structural and functional variation of the interconnecting loop. **(a)** Surface representation of *At*CRY2$_t$ monomer (light blue) and connector region of PHR domain is highlighted in red. Helices are shown as cylinders **(b)** Superposition of connector regions of *At*CRY2$_t$ (red) and active mutant *Zm*CRY1C^{W368A} (blue, PDB: 6LZ3); 0.8Å r.m.s deviation is calculated by PyMOL **(c)** Comparison of connector region of *At*CRY2$_t$ (red) with *At*CRY1 (green, PDB: 1U3C), *At*CRY2$_m$ (yellow, PDB: 6K8I), and *At*CRY2$_i$ (Magenta, PDB: 6K8K); r.m.s deviation of 1.65 Å , 1.49 Å and 1.78 Å respectively are calculated by PyMOL. **(d)** Sidechain view of connector loop region of *At*CRY2$_t$ (red) and *At*CRY2$_m$ (yellow, PDB: 6K8I). **(e)** Sequence alignment and conservation of CRYs interconnecting loop. Residues are colored by traditional amino acid properties in RasMol colors. Arrows indicate residues highlighted in **a-d**.

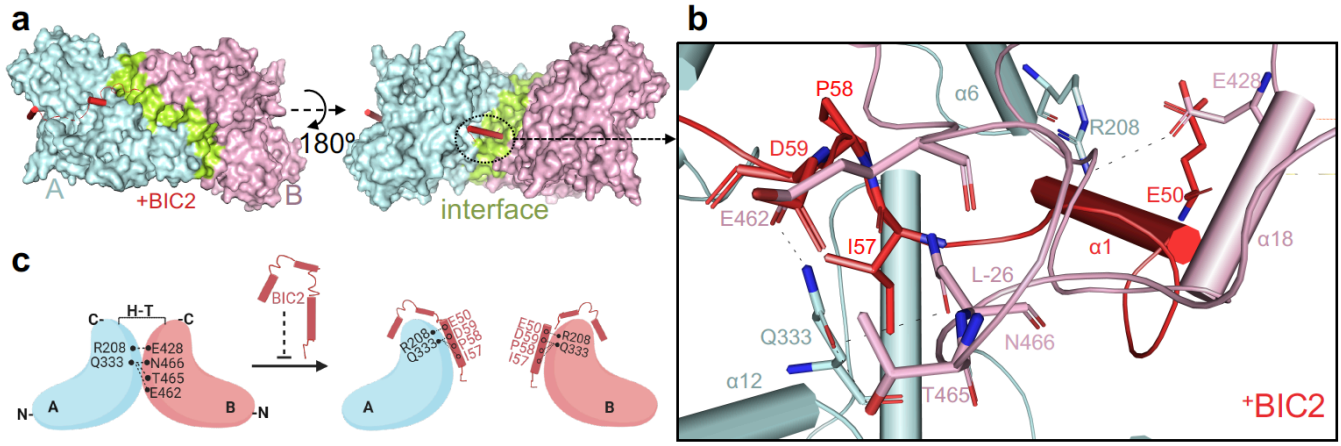

Figure 4. BIC2 disrupts oligomeric formation. (a) Modeling of *At*CRY2$_t$ complexed with *At*BIC2 (red) (superposition of *At*CRY2$_t$ with *At*CRY2$_i$-BIC2 complex, PDB: 6K8K). Monomers A and B are colored in cyan and pink respectively. H-T interface is shown in green. **(b)** Close-up view of BIC2 (red) disrupting H-T interface. Amino acid residues are labeled and colored as indicated in **(a)**. **(c)** Proposed model of BIC2 inhibition (prepared by BioRender).

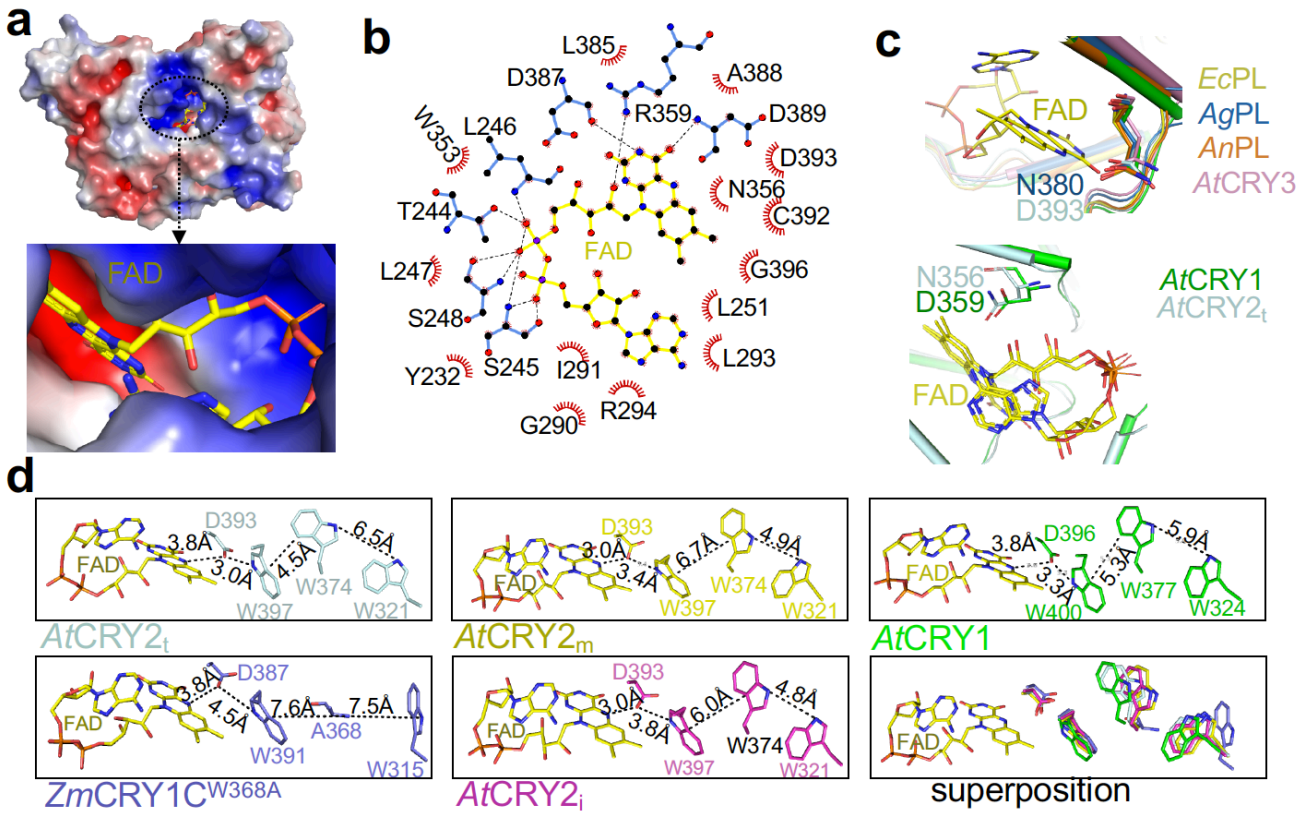

Figure 5. Structural analyses of FAD binding pocket and tryptophan (Trp) triad. (a) Electrostatic surface representation of *At*CRY2$_t$ and close up of FAD (yellow) binding cavity. Electrostatic potential is color coded on the surface with red and blue representing areas of negative and positive charges respectively. **(b)** Interactions of *At*CRY2$_t$ with FAD. FAD in yellow is colored with carbon (black), nitrogen (blue) and oxygen (red). Dotted lines in black represent hydrogen bonds between *At*CRY2$_t$ and FAD. Hydrophobic interactions are shown as spoked arcs (red) (prepared by LigPlot). **(c)** Close up view of FAD (yellow) and diverged residues within the binding pocket of *At*CRY2$_t$ (D393, light blue) superposition with *At*CRY1 (D396, green, PDB: 1U3C), *Arabidopsis, At*CRY3 (N428, Magenta, PDB:2VTB), *Agrobacterium tumefaciens* Photolyase, *Ag*PL (N380, blue, PDB:4U63)[1], *Escherichia coli* Photolyase, *Ec*PL (N378, Yellow, PDB: 1DNP)[2] and *Anacystis nidulans* Photolyase *An*PL (N386, orange, PDB:1TEZ)[3]. **(d)** Comparative analysis of plant cryptochromes tryptophan triad positions in relation to FAD. Residues are colored as in ***c***. Distances were measured with PyMOL and indicated in dotted lines.

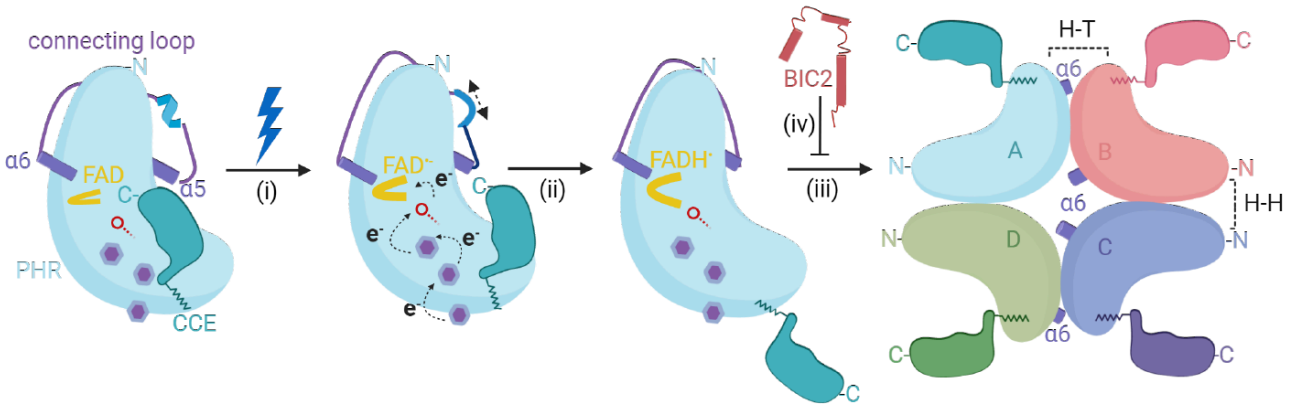

Figure 6. Proposed model of blue light-induced photoactivation and inactivation of plant CRYs. CRYs exist as a monomer non-covalently linked to the oxidized FAD with the CCE tail bound to the PHR domain. The dynamic interconnecting loop in the inactive monomeric state is highlighted in purple with a short α-helix in light blue. **(i)** Blue light illumination causes the FAD to absorb energy and accept electrons *via* the tryptophan triad. The purple benzene rings represent the tryptophans and the red line with an open circle represents amino acid D393. After accepting the electrons, the FAD becomes $FAD^{\bullet-}$ and adopts an open U-shaped conformation followed by an overall change in the conformation of CRY including alterations in the interconnecting loop. **(ii)** The $FAD^{\bullet-}$ becomes neutralized by accepting one proton from D393 and becomes $FADH^{\bullet}$. The overall change in the conformation of the CRY structure induced by photoactivation leads to the loss of secondary structural elements in the interconnecting loop. **(iii)** The photoactivated CRYs adopts an open conformation with CCE tail projecting outward leading to formation of homo-tetramer. The formation of the oligomeric state is guided by the dynamic interconnecting loop that allows the movement of residues in α-6 to participate in forming active interface in the oligomeric state. **(iv)** The photoactivated CRYs are readily inhibited by the presence of BICs which disrupts or prevents the H-T interface in the homo-tetramer.

Table 1. Data collection and refinement statistics

	*At*CRY2$_t$
Data collection	
Space group	P 3_1
Cell dimensions	
a, *b*, *c* (Å)	208.362, 208.362, 81.607
α, β, γ (°)	90, 90, 120
Resolution (Å)	50.05-3.25 (3.36-3.25) *
R_{sym}	0.078 (0.940)
$I / \sigma I$	14.8 (2.2)
Completeness (%)	99.34 (97.64)
Redundancy	1.5 (1.4)
Refinement	
Resolution (Å)	3.25
No. reflections	61839
R_{work} / $R_{free\ (\%)}$	27.1/32.9
No. atoms	15611
Protein	15279
Ligand/ion	302
Water	30
B-factors	53.80
Protein	54.04
Ligand/ion	44.87
Water	19.98
R.m.s. deviations	
Bond lengths (Å)	0.005
Bond angles (°)	1.03
PDB ID	6X24

*Values in parentheses are for highest-resolution shell.